Shi *et al. Microstructures* 2021;1:2021005
DOI: 10.20517/microstructures.2021.04

Microstructures

Research Article

Open Access

Promoting the electrochemical properties of yolk-shell-structured CeO_2 composites for lithium-ion batteries

Yongchao Shi[1], Jipeng Fu[1,2], Kanglong Hui[1,3], Jie Liu[1], Cong Gao[1], Shuqin Chang[1], Yongjin Chen[1], Xiang Gao[1], Tian Gao[3], Ligang Xu[4], Qi Wei[4], Mingxue Tang[1]

[1]Center for High Pressure Science and Technology Advanced Research, Beijing 100094, China.
[2]Key Laboratory of Rare Earth Optoelectronic Materials and Devices of Zhejiang Province, Institute of Optoelectronic Materials and Devices, China Jiliang University, Hangzhou 310018, Zhejiang, China.
[3]Department of Physics, Shanghai University of Electric Power, Shanghai 200090, China.
[4]College of Materials Science and Engineering, Beijing University of Technology, Beijing 100124, China.

Correspondence to: Prof. Mingxue Tang, Center for High Pressure Science and Technology Advanced Research, Build 8, No. 10 Xibeiwang East Rd, Haidian District, Beijing 100094, China. E-mail: mingxue.tang@hpstar.ac.cn; Prof. Jipeng Fu, Center for High Pressure Science and Technology Advanced Research, Build 8, No. 10 Xibeiwang East Rd, Haidian District, Beijing 100094, China. E-mail: fujipeng_7709@163.com

How to cite this article: Shi Y, Fu J, Hui K, Liu J, Gao C, Chang S, Chen Y, Gao X, Gao T, Xu L, Wei Q, Tang M. Promoting the electrochemical properties of yolk-shell-structured CeO_2 composites for lithium-ion batteries. *Microstructures* 2021;1:2021005. https://dx.doi.org/10.20517/microstructures.2021.04

Received: 30 Jul 2021 **First Decision:** 27 Aug 2021 **Revised:** 2 Sep 2021 **Accepted:** 8 Sep 2021 **Available online:** 23 Sep 2021

Academic Editor: Shujun Zhang **Copy Editor:** Xi-Jun Chen **Production Editor:** Xi-Jun Chen

Abstract

Lithium-ion batteries offer significant convenience to modern portable technology and our daily lives due to their high energy density and cycling capabilities. Cerium oxides are attracting significant attention as Li-ion battery anode materials due to their nontoxicity and fast redox kinetics. However, these anodes face critical issues, such as poor electronic conductivity and serve volume expansion upon Li-ion intercalation. Herein, yolk-shell-structured CeO_2 encapsulated in mesoporous carbon nanospheres (CeO_2@void@C) is proposed with an adjustable void between the CeO_2 core and the outer carbon layer. A significantly enhanced capacity and rate performance are obtained for the target CeO_2@void@C when compared with the untreated CeO_2 anode. The reversible capacity of CeO_2@void@C is double that of the untreated CeO_2 anode. Additionally, the yolk-shell-structured CeO_2 shows a slow capacity decay and maintains a capacity of 210 $mAh{\cdot}g^{-1}$ at a current density of 1000 $mA{\cdot}g^{-1}$ with a ~100% Coulombic efficiency even after 1000 cycles. This improvement originates from the conductivity of the coating carbon layer and the void that constrains the volume change upon electrochemical lithiation/delithiation.

Keywords: Li-ion batteries, microstructures, volume constraints, yolk-shell structures, anode materials, CeO_2 composites

INTRODUCTION

With the development of society, carbon neutralization has been augmented immensely due to the consumption of fossil fuels and climate change. There are significant demands for the development of renewable energy and storage technologies. Among the various energy storage systems, lithium-ion batteries (LIBs) are considered as promising energy storage devices due to their high energy density and specific power and long cycle life[1-4]. Rapid charging/discharging technology is currently being increasingly investigated worldwide, which makes the development of new LIBs that provide stable cyclic stability and fast rate capability increasingly more urgent[5,6]. However, it is difficult to satisfy these requirements since traditional graphite is limited by a theoretical specific capacity of only 372 $mAh \cdot g^{-1}$. Simultaneously, the capacity of batteries with graphite anodes rapidly decreases to ~66% after 100 cycles[7]. The demands of high electrochemical performance have engendered the search for alternative anode materials, including carbonaceous materials[8-11], carbon-silicon composites[12,13] and transition metal compounds[14-19]. Rare earth anode materials have also been widely investigated because of their low redox voltage, high cycling rates and other promising properties[20-22].

Cerium oxide (CeO_2) has been widely explored in the fields of supercapacitors, LIBs, catalytic supports in fuel cells and gas sensors[23-25] due to its oxygen deficiency and the fast mutation between Ce(III) and Ce(IV)[26-28]. Bare CeO_2 films[29], core-shell nanospheres[27], hollow spheres[30] and CeO_2/carbon composites[31] have all been investigated as LIB anodes. The basic working mechanism of cerium oxide in a LIB charge/discharge procedure can be described as[27]:

$$2CeO_2 + 2Li^+ + 2e^- \Leftrightarrow Ce_2O_3 + Li_2O$$

However, the main residual issues of cerium oxide as an anode material are low electronic conductivity and a crystal structure crushing (shatter effect) during cycling. To solve these issues, researchers have dedicated considerable effort to constructing composites with materials such as carbon-coated TiO_2[32,33], SnO_2[34-36] and Fe_3O_4[37,38] to markedly enhance the electrochemical properties of cerium oxide. Structures compounded with carbon can effectively confine the matrix to alleviate volume changes and obstruct the aggregation of active particles. For oxide and sulfide anodes, due to the prominent volume expansion during Li^+ intercalation/deintercalation, the use of core-shell structures may result in stress fractures and exfoliation[27]. Inspired by previous studies, an attractive strategy to fabricate yolk-shell structures with tunable void spaces was proposed for CeO_2 with the aid of an outer carbon layer to avoid damage to the architecture[39].

In this contribution, we report the design and synthesis of yolk-shell-structured CeO_2@void@C using a self-template strategy method. First, uniform CeO_2 nanospheres are synthesized from a solvothermal method. A layer of SiO_2 is then coated on the surface of CeO_2 to form CeO_2@SiO_2, which is further solved in a resorcinol formaldehyde (RF) solution to obtain core-shell-structured CeO_2@SiO_2@RF. By annealing and etching, the target CeO_2@void@C is obtained and fully characterized by structural determination and electrochemical investigations. The electrochemical performance of CeO_2@void@C is demonstrated according to its well-designed nanoarchitecture. The electrochemical reaction mechanisms are probed by X-ray diffraction (XRD) and nuclear magnetic resonance (NMR) spectroscopy.

MATERIALS AND METHODS

Materials

The raw materials of cerium carbonate hexahydrate [$Ce_2(CO_3)_3{\cdot}6H_2O$], ethylene glycol $(CH_2OH)_2$, ethanol (ETOH), glacial acetic acid (CH_3COOH), sodium citrate ($C_6H_5Na_3O_7$), resorcinol [$C_6H_4(OH)_2$], tetraethylorthosilicate, ammonia solution, formaldehyde and sodium hydroxide solution were purchased from MACKLIN and used without further purification. $LiPF_6$ (1 M), N-methyl-2-pyrrolidine, polyvinylidene fluoride and a Celgard 2400 separator were used for the electrochemical experiments.

Sample preparation and characterization

Synthesis of yolk-shell-structured CeO_2@void@C nanospheres

Initially, uniform CeO_2 nanospheres were synthesized by a hydrothermal method and adopted as the initial materials. Typically, 1 g of $Ce_2(CO_3)_3{\cdot}6H_2O$ was dissolved in 1 mL of deionized water, with 1 mL of glacial acetic acid, 0.1 g of sodium citrate and 30 mL glycol then added. The mixture was stirred for 30 min and then transferred to a Teflon-lined hydrothermal autoclave, which was heated at 180 °C for 4 h. The product was washed with ethanol and deionized water three times and placed in a blast drying oven at 60 °C for 12 h to obtain the homogenous CeO_2 nanospheres.

The yolk-shell-structured CeO_2@void@C was prepared using the following steps. First, 0.1 g of CeO_2 nanospheres were dispersed in a 140 mL ethanol-water (1:6) solvent mixture via ultrasonic treatment for 30 min. Then, 3 mL of NH_4OH (28 wt.%) and 0.5 mL of tetraethyl orthosilicate were added, followed by stirring for an additional 6 h. Afterwards, the CeO_2 particles were coated by a SiO_2 layer, followed by centrifugal action, washing and drying at 60 °C for 12 h. Next, 0.1 g of CeO_2@SiO_2 were dispersed in a 100 mL ethanol-water (1:4) solvent and a homogeneous mixture was generated by ultrasound treatment for 30 min. Then, 0.1 g of resorcinol and 3 mL of NH_4OH reagent were added and subsequently stirred for 30 min. This was followed by the addition of 0.05 mL of formaldehyde into the mixed solution to react under continuous stirring for 6 h. The final product was further dried at 60 °C for 12 h to obtain CeO_2@SiO_2@RF. A condensed layer of SiO_2 and a polymeric layer of RF were coated onto CeO_2 via a successive sol-gel process. The carbon layer was coated on CeO_2@SiO_2 using RF as a precursor by annealing under an inert atmosphere (N_2). The procedure of making yolk-shell-structured CeO_2@void@C is illustrated in Figure 1. Finally, the uniform yolk-shell-structured CeO_2@void@C was obtained by etching off the sacrificial SiO_2 layer with a sodium hydroxide solution.

Structure and morphological characterization

Crystal structures were determined using a PANalytical Empyrean X-ray diffractometer. The morphologies were characterized by scanning electron microscopy (SEM) with a JSM-7900F field emission scanning electron microscope. Thermogravimetric analysis (TGA) was performed on a Netzsch STA449 F5/F3 Jupiter thermal analyzer. The Raman spectra were determined using an inVia™ confocal Raman microscope. The specific surface area and aperture of the samples were measured by an ASAP2460 physical adsorption analyzer. The chemical states of the samples were studied with X-ray photoelectron spectroscopy (XPS) using a Thermo ESCALAB 250xi. The microscopic crystal structures were characterized using transmission electron microscopy (TEM) with a JEM-F200 field emission transmission electron microscope. Solid-state ^{7}Li NMR spectra were measured on a Bruker spectrometer with a ^{7}Li Larmor frequency of 155.52 MHz. All cycled anodes were packed into 4 mm rotors in an Ar glovebox. The samples were spun at a magic angle spinning rate of 8 or 10 kHz to assign the isotropic signal. The recycle delay d_1 was set to 6 s and the single 90° pulse length was 2.6 μs at a power of 300 W. Shifts were externally referenced to the 0-ppm peak of a 1 M LiCl solution. The spin-lattice relaxation times (T_1) were determined using the inverse recovery technique. The spectra were analyzed according to Dmfit[40].

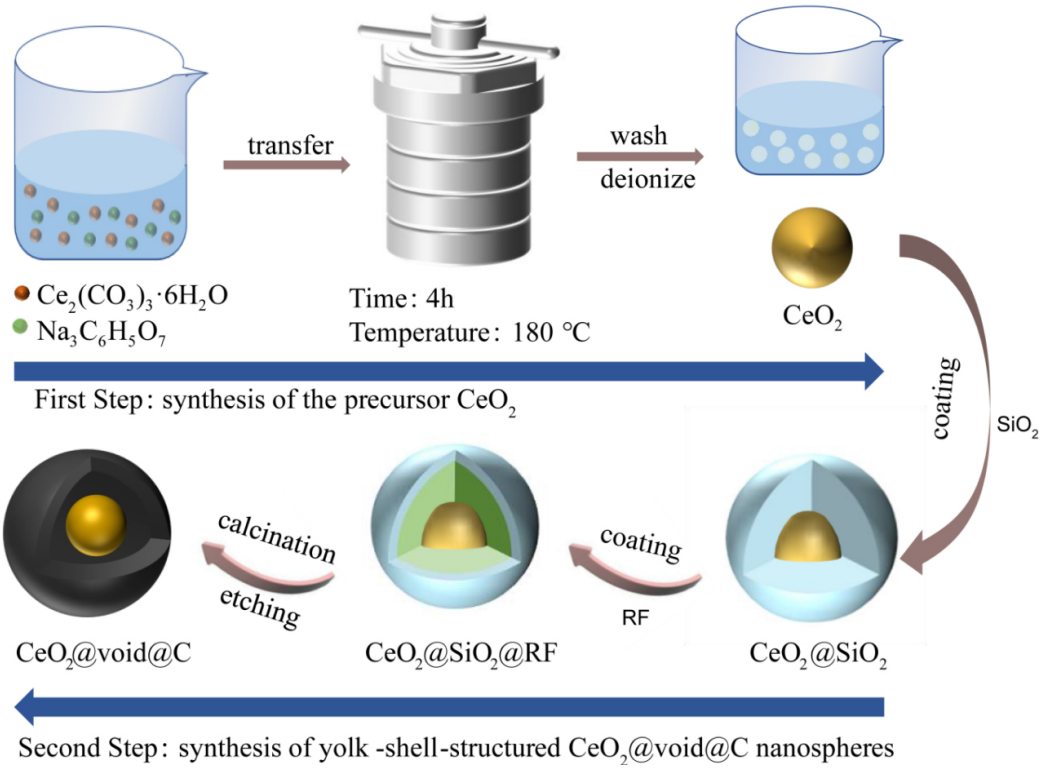

Figure 1. Schematic of preparation process for yolk-shell-structured CeO_2@void@C nanospheres.

Electrochemical characterization

Lithium foil was employed as the counter electrode for the evaluation of the electrochemical performance. The active materials (yolk-shell-structured CeO_2@void@C or bare CeO_2), conductivity agent (Super P) and polyvinylidene fluoride in a weight ratio of 60:30:10 were mixed with the N-methyl-2-pyrrolidine solvent to generate a homogenous slurry. It was then painted onto Cu foil and dried at 80 °C overnight under a vacuum. $LiPF_6$ (1 M) was solved in diethyl carbonate/dimethyl carbonate/ethylene carbonate (1:1:1 vol.%) with the addition of 10 wt.% fluorinated ethylene carbonate to serve as the electrolyte. Celgard 2400 was used as the separator. The batteries were assembled in CR2032 coin cells. The electrochemical performance was studied through a Lanthe CT2001A/B testing system. Electrochemical impedance spectroscopy (EIS) was carried out using an SP-150 workstation (BioLogic, France).

RESULTS AND DISCUSSION

To make the synthesis procedure clearer, the complete routine is presented in Figure 1. First, CeO_2 nanoparticles were obtained using a solvothermal method, in which the homogenous mixture of $Ce_2(CO_3)_3 \cdot 6H_2O$ and $Na_3C_6H_5O_7$ was kept at 180 °C for 4 h. A layer of SiO_2 was then coated onto the as-synthesized CeO_2 via a sol-gel method to form CeO_2@SiO_2, which was further coated with RF to produce the core-shell structure of the CeO_2@SiO_2@RF nanospheres. Finally, the outer RF was annealed to the carbon layer and the interlayer of SiO_2 was etched to form CeO_2@void@C with a yolk-shell structure.

XRD was performed to determine the crystal structures of the as-synthesized materials. Cubic CeO_2 nanospheres were successfully synthesized according to the XRD patterns [Figure 2A], in which the peaks at 28.6°, 33.1°, 47.5° and 56.3° correspond to the (111), (200), (220) and (311) crystal faces, respectively. No position shifts were observed for pure CeO_2 or CeO_2@void@C, indicating that the coating treatment does

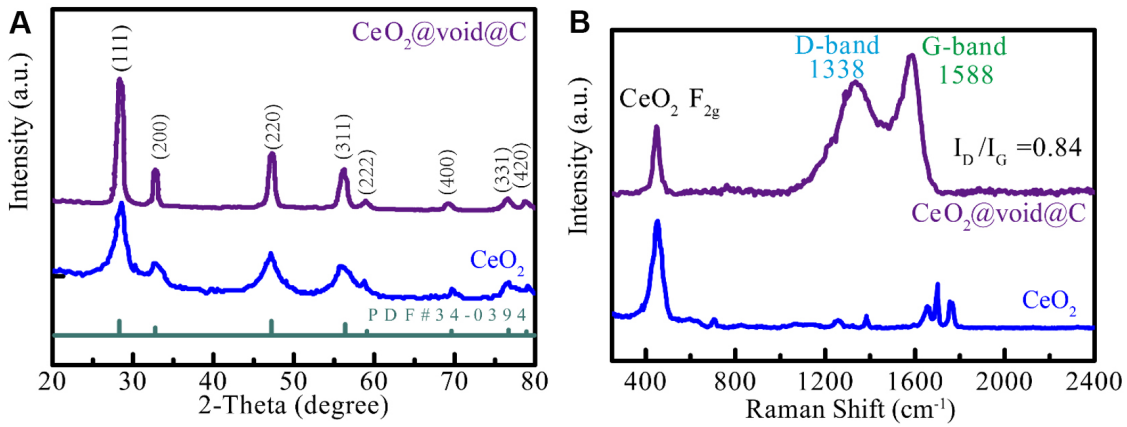

Figure 2. (A) X-ray diffraction patterns of untreated CeO_2 and CeO_2@void@C. (B) Raman spectra of CeO_2 and CeO_2@void@C.

not influence the lattice parameters of the CeO_2 core. However, all the peaks became sharper for the yolk-shell-structured CeO_2@void@C, which should be attributed to the annealing process at 600 °C, resulting in a better crystalline phase. Additionally, there is no diffraction peak detected for carbon, revealing that the coating layer is amorphous. The Raman spectra of CeO_2 and CeO_2@void@C were also characterized [Figure 2B]. The peak at 460 cm^{-1} for the characterization of the F_{2g} vibration was detected for both CeO_2 and CeO_2@void@C[27]. For the yolk-shell-structured CeO_2@void@C, two extra intensive broad peaks at 1338 and 1588 cm^{-1} were observed, which could be assigned to the D band (disorder induction) and G band (graphite), respectively. The intensity ratio of the D and G bands (I_D/I_G) was referenced to evaluate the graphitization degree[5]. The I_D/I_G ratio was calculated as ~0.844 for CeO_2@void@C, which reveals good graphitization and electronic conductivity, resulting in faster cycling rate performance of CeO_2@void@C when compared with the untreated CeO_2.

The morphologies of CeO_2 and CeO_2@void@C are displayed in Figure 3 and are homogeneously distributed in size. As shown in Figure 3A and C, the particle diameters of both CeO_2 and CeO_2@void@C are ~100 and ~220 nm, respectively. The tapped density of the anode has a certain impact on the performance and specific capacity and depends on the intrinsic density and particle size distribution. A higher intrinsic density and narrower particle size distribution result in a higher tapped density. Although there is a certain space between the core and shell, the high density core and homogeneous particle size ensure good tapped density. The good tapped capacity could be further improved by optimizing the void volume between the CeO_2 core and the carbon shell. The etching and annealing process does not change the size of the carbon coating layer when compared to Figure 3B and C. The high-resolution TEM images of pure CeO_2 are shown in Figure 3E.

The lattice fringe spacing of CeO_2 is in good agreement with the XRD patterns [Figure 2]. The energy dispersive X-ray spectrum elemental mapping images indicate that Ce and O are homogenous for CeO_2 [Figure 3F]. Obviously, there is no signal for carbon in the CeO_2 sample. With regards to the CeO_2@void@C sample, the carbon coating layer is determined as being ~20 nm thick, as shown in Figure 3G. An obvious void space is found between the CeO_2 core and the carbon layer [Figure 3C and G]. Due to the shielding of the carbon layer, the lattice fringe is not clear for the coated CeO_2@void@C [Figure 3H]. The elemental mappings show that both Ce and O are localized within the CeO_2 core [Figure 3I], while carbon is distributed at the outer layer. To check the stability of the structure, cycled samples were also measured. CeO_2@void@C maintains good morphology after cycling [Supplementary Figure 1]. However, the CeO_2 nanoparticles without the carbon shell agglomerated badly after 100 cycling scans [Supplementary Figure 2].

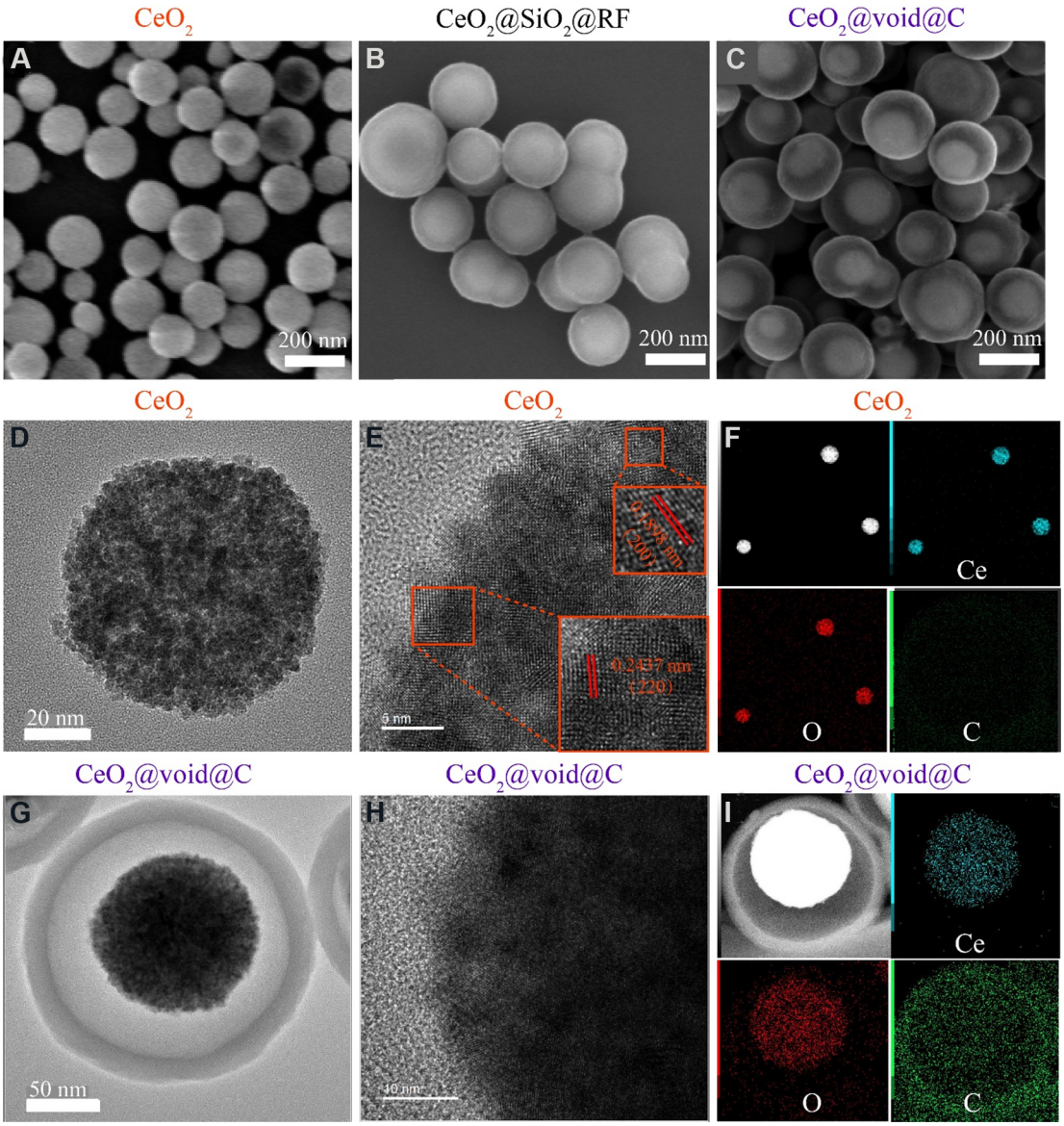

Figure 3. Scanning electron microscopy images of (A) CeO_2, (B) CeO_2@SiO_2@RF and (C) CeO_2@void@C. High-resolution transmission electron microscopy images of (D, E) CeO_2 and (G, H) CeO_2@void@C. EDS elemental maps of (F) CeO_2 and (I) CeO_2@void@C.

The surface area and pore size distribution were determined by nitrogen adsorption-desorption isotherms. The specific surface of the untreated CeO_2 [Figure 4A] is only 26 $m^2 \cdot g^{-1}$ and was obtained by the Brunauer-Emmett-Teller method. In comparison, the specific surface area increases profoundly to 166 $m^2 \cdot g^{-1}$ [Figure 4B] for CeO_2@void@C, which obviously exhibits typical type IV isotherms for the mesoporous structures of the carbon layer. The higher specific surface of CeO_2@void@C means more active sites for lithium accommodation, thereby offering a larger capacity as a LIB anode. Moreover, the pore size of CeO_2@void@C was calculated via the Barrett-Joyner-Halenda method [Figure 4C], which shows a narrow pore size distribution centered at ~7.6 nm. TGA was also carried out to check the stability of the obtained material, as shown in Figure 4D. CeO_2@void@C shows good thermal stability below 370 °C but experiences a large mass loss between 370 and 500 °C due to the decomposition of the carbon layer. The carbon content is calculated as ~28 wt.% in the total yolk-shell-structured CeO_2@void@C.

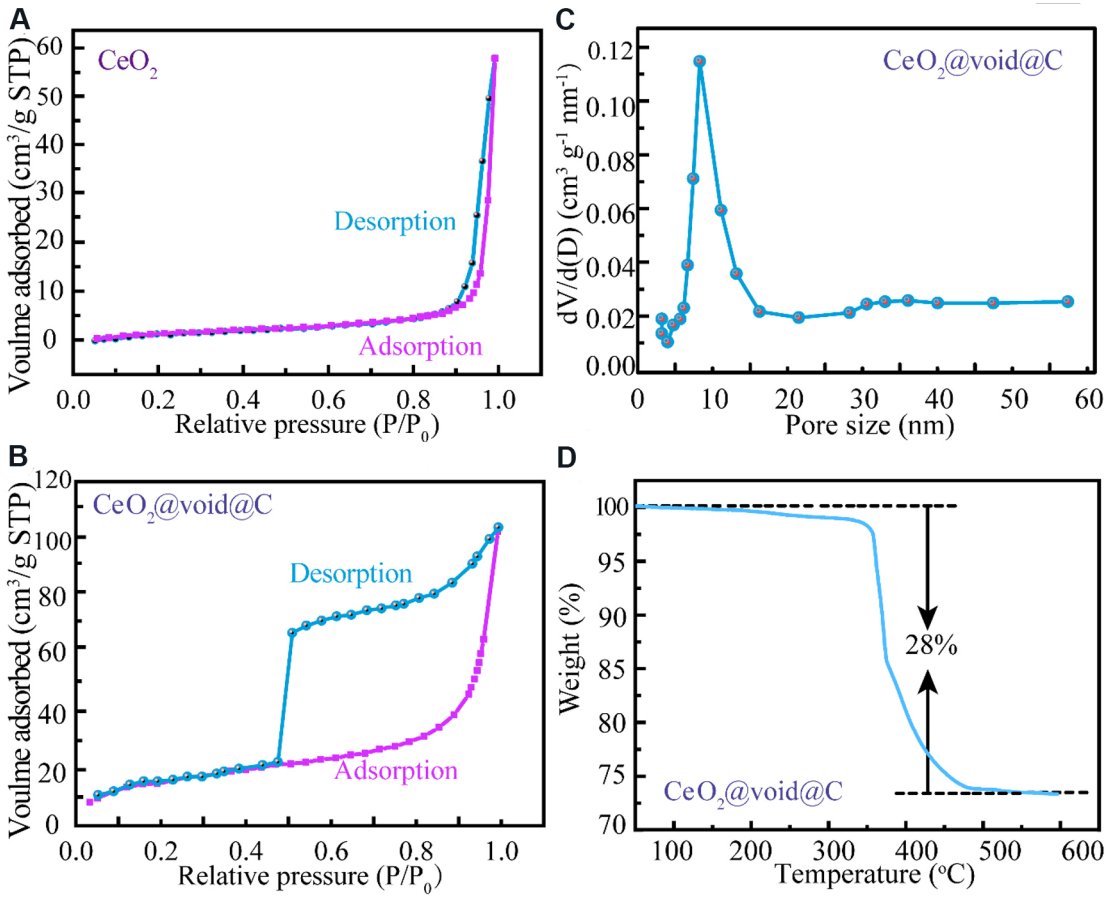

Figure 4. N_2 adsorption-desorption isotherms of as-prepared CeO_2(A) and CeO_2@void@C (B). (C) Pore size distribution of CeO_2@void@C. (D) Thermogravimetric analysis curve of CeO_2@void@C.

XPS was carried out to investigate the surficial elements and valence states of CeO_2@void@C. All signals of Ce, O and C appear in the full spectrum [Figure 5A]. For the CeO_2@void@C [Figure 5B], the XPS spectrum of Ce 3d included five peaks of Ce 3d3/2 and three peaks of Ce 3d5/2[41]. Based on the signal integration of Ce 3d5/2, the peaks of Ce^{4+} are located at 879.8 and 886.5 eV, while one peak of Ce^{3+} is located at 883.0 eV. The corresponding areas were integrated and the ratio of Ce^{3+} and Ce^{4+} is 31:69, which could be approximated as the atomic fractions in redox states. The Ce 4d peak in the full survey also belongs to Ce_2O_3, proving the existence of Ce^{3+} in CeO_2. Therefore, the redox state of Ce in the as-prepared CeO_2@void@C nanospheres is both tetravalent and trivalent.

The electrochemical properties were fully investigated for the in-depth study of the potential application and mechanism of CeO_2@void@C. Figure 6A shows the cyclic voltammetry (CV) analysis of CeO_2@void@C at a scan rate of 0.1 $mV \cdot s^{-1}$ in the voltage range of 0.01 to 3.00 V. In the first cathodic polarization process, two broad cathodic peaks were observed. The first cycle is partially irreversible because of side reactions, such as electrolyte decomposition and the formation of a solid electrolyte interface (SEI) film. The cathodic peak (1.24 V) was observed only in the first cycle, which can be attributed to the initial insertion of Li ions and the breakdown of electrolytes. After the first cycle, the following cathodic peak located between 0.8 and 0.1 V may be ascribed to the reductive transformation of CeO_2 to Ce_2O_3 and Li_2O according to the conversion reaction. The CV curves quickly become stable and the discharge-charge curves almost overlap with each other, indicating that the electrochemical reactions are highly reversible for CeO_2@void@C.

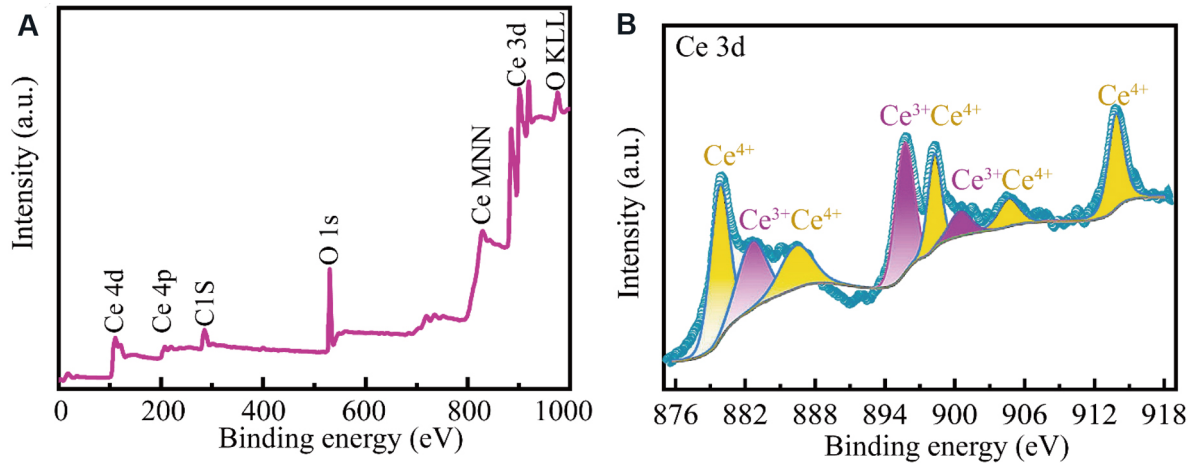

Figure 5. (A) Full X-ray photoelectron spectroscopy (XPS) spectrum of CeO_2@void@C. (B) High-resolution XPS spectrum and simulation of Ce 3d for CeO_2@void@C.

Figure 6B shows the first three electrochemical cycles of a Li//CeO_2@void@C battery at a current density of 100 mA·g^{-1}. The initial discharge and charge capacities were characterized as 615 and 321.13 mAh·g^{-1}, respectively, with a Coulombic efficiency of 51.38%. The initial irreversible capacity loss is mainly due to the electrolyte decomposition, the formation of an SEI film and the irreversible formation of Li_2O. During the second and third circles, the discharge and charge contours are almost identical, reflecting the excellent structural stability of the electrode. Figure 6C compares the rate performances of the untreated CeO_2 and the CeO_2@void@C electrodes. With increasing current density from 100 to 200, 500 and 1000 mA·g^{-1}, the Li//CeO_2@void@C battery delivered reversible discharge capacities of 313, 265, 227 and 196 mAh·g^{-1}, respectively. For the Li//CeO_2 battery, the capacities are determined only as 104.8, 84.1, 61.2 and 50 mAh·g^{-1} under the corresponding current densities. The capacity of the Li//CeO_2@void@C battery was maintained at ~300 mAh·g^{-1} and 100 mAh·g^{-1} was recovered for the Li//CeO_2 battery when the current density was restored to 100 mAh·g^{-1}. Along with all different applied currents, the capacities of CeO_2@void@C are almost three times those obtained for the untreated CeO_2.

EIS of CeO_2@void@C and untreated CeO_2 was performed to determine their resistance and diffusion behavior [Figure 6D]. The impedance data were fitted as an equivalent electrical circuit, which is composed of the solution resistance (Rs), the charge transfer resistance (Rct), the constant phase element and the Warburg impedance (Rw)[42]. The analyzed impedance results are listed in Table 1. The values of Rct for the CeO_2@void@C anode and the untreated CeO_2 anode were calculated to be 232.5 and 464 Ohm, respectively. Obviously, faster kinetics in the electrochemical reactions exist for the CeO_2@void@C anode compared to the untreated CeO_2. The total resistance of CeO_2 is larger than that of the CeO_2@void@C as an electrode. The long-term cycling performance was also tested [Figure 6E] and the capacity gradually decreases from ~300 to ~200 mAh·g^{-1} at a current density of 100 mAh·g^{-1} after 1000 cycles. The initial 50 cycles are shown in Supplementary Figure 3 for better comparison. Surprisingly, CeO_2@void@C shows an excellent Coulombic efficiency of 100% due to the structural stability endowed by the buffer space.

To understand the electrochemical mechanism of the CeO_2@void@C anode, CV was carried out under different rates, as shown in Figure 7A. The storage mechanism is manipulated by two types of process, namely, diffusion-controlled behavior and pseudocapacitive storage, which can be estimated by the ratio of the square root of current and the scan rate as the factor of b values[43,44]. The process is completely controlled by ion diffusion when b is 0.5, while the capacitance effect dominates when b is 1. As shown in

Table 1. Impedance parameters calculated from EIS

Material	Rs (Ohm)	Rct (Ohm)
Bare CeO_2	49.7	464
CeO_2@void@C	2.9	232.5

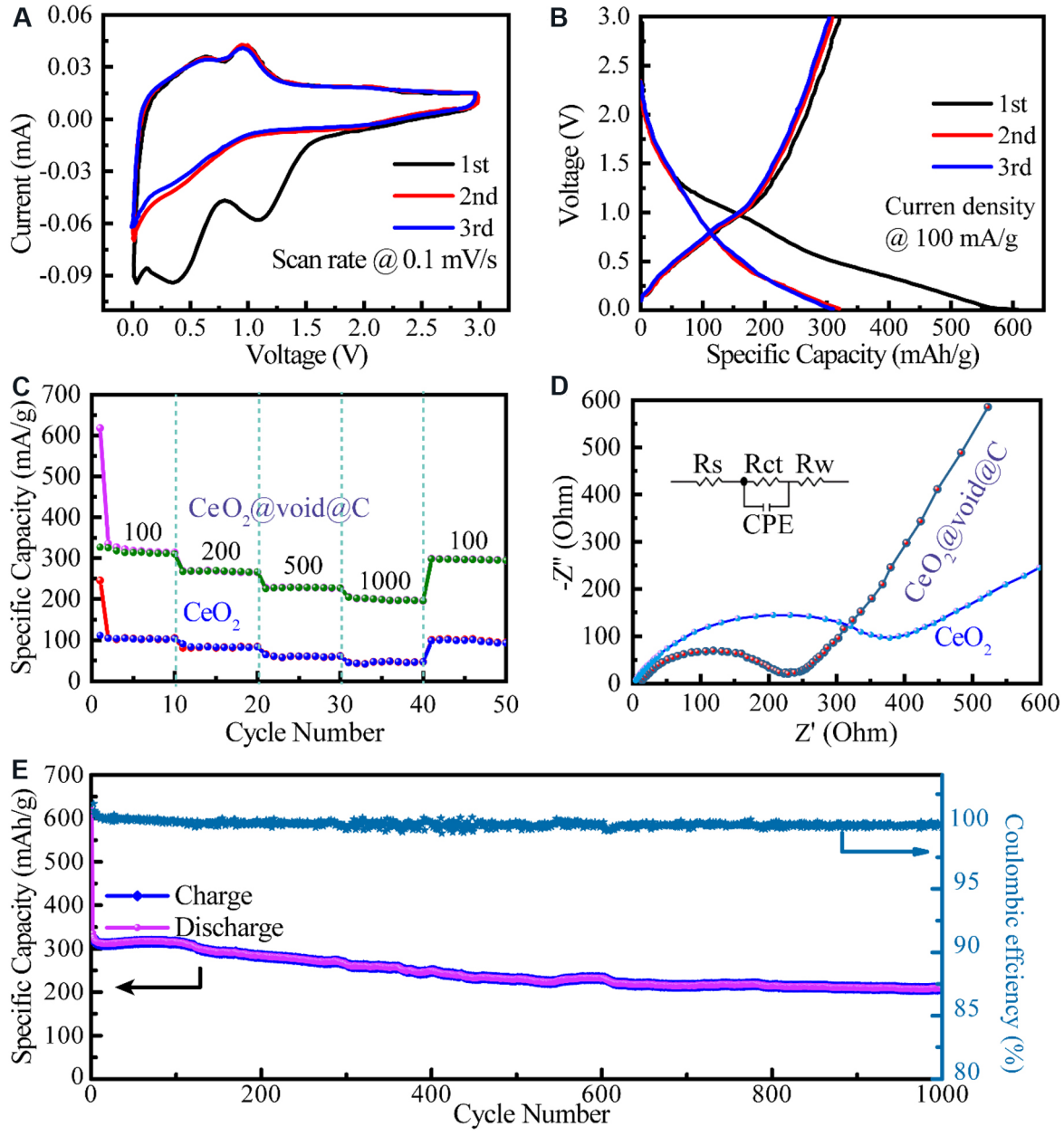

Figure 6. (A) Cyclic voltammetry of CeO_2@void@C at a scan rate of 0.1 mV·s^{-1} at room temperature. (B) Cycling performance of CeO_2@void@C. (C) Rate performance of untreated CeO_2 and CeO_2@void@C under different applied current densities, whose values are marked in columns in mA·g^{-1}. (D) Nyquist impedance curves for the untreated CeO_2 and CeO_2@void@C materials. (E) Long life cycling performance of CeO_2@void@C under a current density of 0.1 A·g^{-1}.

Figure 7B, b values of 0.93 and 0.84 are determined for peaks 1 and 2, respectively, revealing a pseudocapacitive behavior for CeO_2@void@C. A pseudocapacitive contribution of 77.3% at a 0.8 mV·s^{-1}

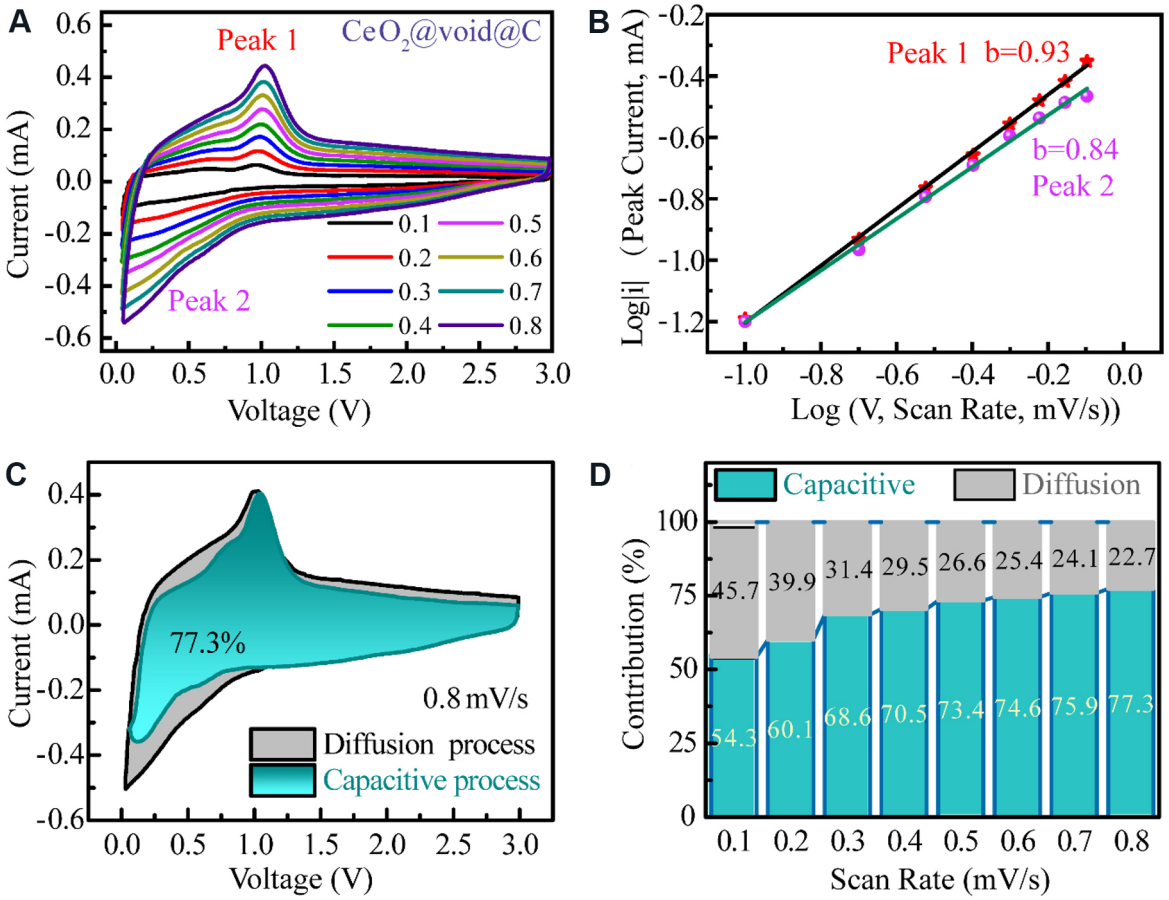

Figure 7. (A) Cyclic voltammetry curves of CeO_2@void@C electrode under different scan rates. (B) Fitting of the square root of the peak current and the scan rate ($v^{1/2}$). (C) Capacitive contribution of CeO_2@void@C to the total storage. (D) Contribution ratios of the capacitive and diffusion-controlled process under various scan rates.

scanning rate is determined for the CeO_2@void@C anode, as calculated in Figure 7C. By varying the scan rate [Figure 7D], the pseudocapacitive contributions are 54.3%, 60.1%, 68.6%, 70.5%, 73.4%, 75.9% and 77.3% under scanning rates of 0.1, 0.2, 0.3, 0.4, 0.5, 0.6, 0.7 and 0.8 $mV \cdot s^{-1}$, respectively. Therefore, the pseudocapacitive process shows a significant role in the total capacity and its contribution grows with increasing scanning rate.

Ex-situ XRD at the first cycle was carried out to investigate the component and crystal structure variation of CeO_2@void@C. Certain cycling states of the batteries were selected, as marked to the right of Figure 8. The XRD pattern of the pristine anode shows the pure phase of CeO_2. Upon discharge, the diffraction peak slightly shifted to a lower value of 2θ, which is consistent with the peak position trend of Ce_2O_3. Meanwhile, lithium ions are embedded in the lattice, making the lattice parameters larger. Thus, the partial formation of the Ce_2O_3 phase structure and cell volume expansion are confirmed during lithiation. In the subsequent charge process, the peaks inversely move back to larger 2θ values, which could be due to the extraction of Li ions, causing oxidation of Ce^{3+} to Ce^{4+} and cell shrinking. The peak positions of the fully charged sample are still slightly lower than those of the pristine material, which is attributed to the irreversible reaction and residual lithium ions. No new phase was detected in the whole charge/discharge process. Therefore, the electrochemical cycling of the CeO_2@void@C electrode could be considered as an intercalation/extraction reaction process.

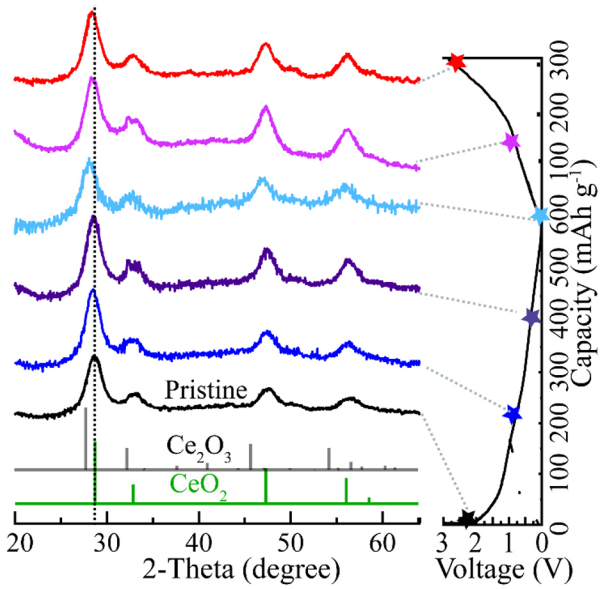

Figure 8. *Ex-situ* XRD of CeO_2@void@C at various cycling states. The corresponding electrochemical curve is displayed to the right. For better comparison, the indexes of both CeO_2 and Ce_2O_3 are also plotted for reference.

NMR is very sensitive to the Li-ion local environment of battery materials[45,46]. The solid-state ^{7}Li NMR spectra of Li_xCeO_2@void@C electrodes at different cycling states are shown in Figure 9. As shown in Figure 9A, all the electrodes show wide spinning sidebands ranging from -600 to 600 ppm because of the anisotropy of Li, together with the possible hyperfine interaction between the unpaired electrons of $Ce^{3+/4+}$. The electrode discharged to 1.1 V (bottom spectrum in Figure 9A) presents a sharp symmetric peak at -0.4 ppm for isotropic resonance. With further lithiation to 0.4 V, the isotropic peak becomes broader with a shift to a low field. At the end of discharge to 0.01 V, an even broader signal is observed. Reversible evolution is observed when delithiation takes place.

For a clearer discussion, the spectra are simulated and the deconvoluted spectra of the isotropic resonances are presented in Figure 9B. For the electrode discharged to 1.1 V, only one peak at -0.4 ppm is simulated, which is possibly originated from the SEI components, such as LiF and Li_2CO_3[47]. When the anode is further discharged to 0.4 V, an additional peak at 2 ppm with 41% occupancy appears in addition to the first peak at -0.4 ppm, which accounts for 59%. The signal at 2 ppm is mainly assigned to the product Li_2O. Deeper lithiation to 0.01 V produces an extra signal at even downfield to 8 ppm, with an occupancy of 32%. The change of Fermi contact along the Ce-O-Li bond is the main reason for the spectral shifts, as the electron cloud varies due to the reduction of Ce^{4+} to Ce^{3+} upon discharge, or different sites/vacancies are occupied by the intercalated Li^+. Upon subsequent charge, a reverse trend is observed. When the electrode is charged to 1 V, the signals at 8 and 2 ppm decrease to 7% and 37% from 32% and 47%, respectively. When the battery is further charged to 3 V, the signal at 8 ppm disappeared completely and 10% is still residual for the signal at 2 ppm caused by the irreversible reaction. Furthermore, the relaxation time T_1 decreases upon discharge due to the reduction of Ce^{4+} to Ce^{3+}, with the latter displaying stronger paramagnetization. This is regained upon the following charge because of reverse evolution. The NMR results are in good agreement with the above-mentioned XRD study.

CONCLUSIONS

In summary, yolk-shell-nanostructured CeO_2@void@C was designed and its electrochemical properties

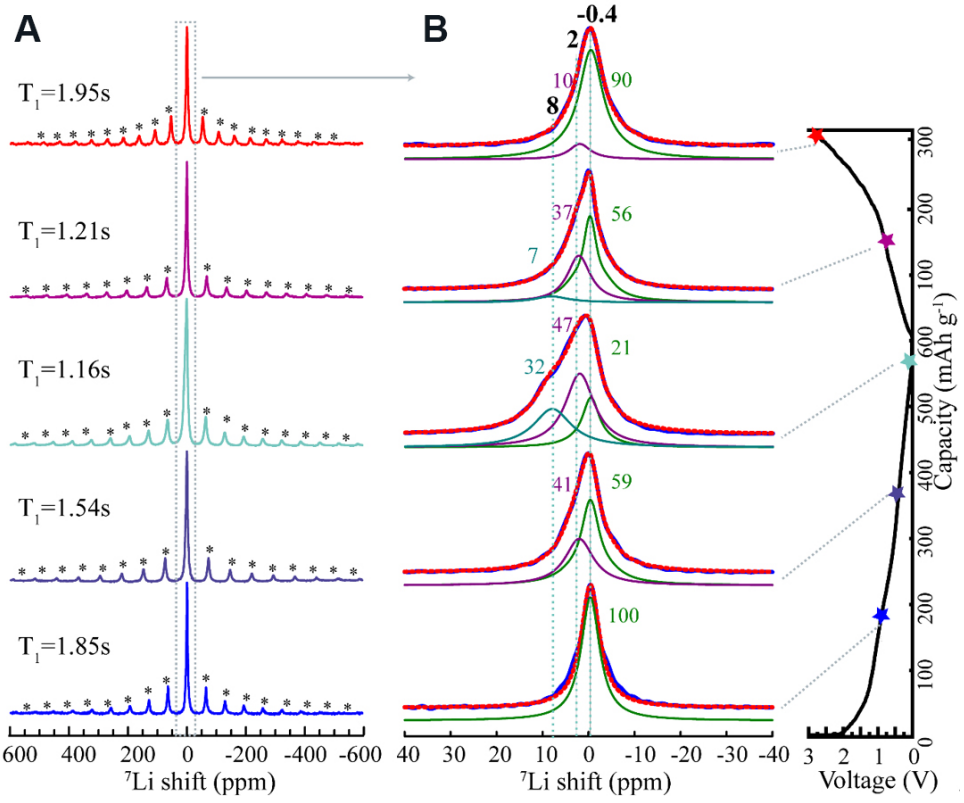

Figure 9. Solid-state ^{7}Li NMR spectra of cycled CeO_2@void@C electrodes at different states. (A) Full spectra with the spinning sidebands marked with asterisks. The corresponding longitudinal relaxation time T_1 is noted to each spectrum. (B) The simulation region of the isotropic signal is marked by the rectangular dotted frame, as shown in (A). Blue signals are obtained from experiment and red-dashed curves are the sum of deconvolution. The chemical shifts and occupancies are marked for each simulated peak.

were fully investigated as an anode for LIBs. Both good electronic conductivity and enhanced capacity were achieved according to the hollow carbon shell composite structure of CeO_2@void@C. Furthermore, the excellent cycling stability was further confirmed by the fast charge transfer and long-term cycling test. The structure-property correlation proposes a promising strategy for fabricating nanosized CeO_2 cores and carbon shells with adjustable voids, which show enhanced lithium storage properties. XRD and NMR analysis reveals that the intercalation process dominates the lithiation/delithiation reaction for the CeO_2@void@C anode, which is consistent with the pseudocapacitance storage mechanism for CeO_2@void@C. This work may help to design and fabricate hybrid composites for energy storage applications.

DECLARATIONS

Acknowledgments

The authors thank Dr. Yonggang Wang and Dr. Kuo Li for helpful discussion. The platform of HPSTAR is acknowledged.

Authors' contributions

Performed materials synthesis and electrochemical experiments, together with data collection and analysis: Shi Y, Hui K

Made substantial contributions to conception and design of the materials and data analysis and interpretation: Fu J, Tang M

Performed TEM, SEM data acquisition and analysis: Chen Y, Gao C, Gao X
NMR measurements and analysis: Liu J, Chang S, Xu L, Wei Q, Tang M
All authors contribute to the manuscript and are involved in discussion.

Availability of data and materials

Data can be deposited into data repositories or published as supplementary information in the journal.

Financial support and sponsorship

This work was supported by the National Natural Science Foundation of China (Grants 21974007, U1930401 and U1530402) and the Natural Science Foundation of Zhejiang Province (Grant No. LQ21E020006).

Conflicts of interest

All authors declared that there are no conflicts of interest.

Ethical approval and consent to participate

Not applicable.

Consent for publication

Not applicable.

REFERENCES

1. Tarascon J, Armand M. Issues and challenges facing rechargeable lithium batteries. Materials for Sustainable Energy. Co-Published with Macmillan Publishers Ltd, UK; 2010. p. 171-9. DOI
2. Kang K, Meng YS, Bréger J, Grey CP, Ceder G. Electrodes with high power and high capacity for rechargeable lithium batteries. *Science* 2006;311:977-80. DOI PubMed
3. Xu K. Nonaqueous liquid electrolytes for lithium-based rechargeable batteries. *Chem Rev* 2004;104:4303-417. DOI PubMed
4. Whittingham MS. Lithium batteries and cathode materials. *Chem Rev* 2004;104:4271-301. DOI PubMed
5. Xia H, Li K, Guo Y, Guo J, Xu Q, Zhang J. CoS_2 nanodots trapped within graphitic structured N-doped carbon spheres with efficient performances for lithium storage. *J Mater Chem A* 2018;6:7148-54. DOI
6. Wang S, Guan BY, Yu L, Lou XWD. Rational design of three-layered TiO_2 @Carbon@MoS_2 hierarchical nanotubes for enhanced lithium storage. *Adv Mater* 2017;29:1702724. DOI PubMed
7. Lee SM, Kim J, Moon J, et al. A cooperative biphasic MoO_x-MoP_x promoter enables a fast-charging lithium-ion battery. *Nat Commun* 2021;12:39. DOI PubMed PMC
8. Pei F, An T, Zang J, et al. From hollow carbon spheres to N-doped hollow porous carbon bowls: rational design of hollow carbon host for Li-S batteries. *Adv Energy Mater* 2016;6:1502539. DOI
9. Wu J, Rui X, Long G, Chen W, Yan Q, Zhang Q. Pushing up lithium storage through nanostructured polyazaacene analogues as anode. *Angew Chem Int Ed Engl* 2015;54:7354-8. DOI PubMed
10. Zhu Y, Yang M, Huang Q, et al. V_2O_5 textile cathodes with high capacity and stability for flexible lithium-ion batteries. *Adv Mater* 2020;32:e1906205. DOI
11. Wang J, Cui Y, Wang D. Hollow multishelled structures revive high energy density batteries. *Nanoscale Horiz* 2020;5:1287-92. DOI PubMed
12. Xiao Q, Fan Y, Wang X, Susantyoko RA, Zhang Q. A multilayer Si/CNT coaxial nanofiber LIB anode with a high areal capacity. *Energy Environ Sci* 2014;7:655-61. DOI
13. Polat B, Levent Eryılmaz O, Keleş O. Si based anodes via magnetron sputtering for LIB. *ECS Electrochemistry Letters* 2014;3:A45-9. DOI
14. Varghese B, Reddy MV, Yanwu Z, et al. Fabrication of NiO nanowall electrodes for high performance lithium ion battery. *Chem Mater* 2008;20:3360-7. DOI
15. Yu M, Wang A, Wang Y, Li C, Shi G. An alumina stabilized ZnO-graphene anode for lithium ion batteries via atomic layer deposition. *Nanoscale* 2014;6:11419-24. DOI PubMed
16. Wang J, Zhou B, Zhao H, et al. A sandwich-type sulfur cathode based on multifunctional ceria hollow spheres for high-performance lithium-sulfur batteries. *Mater Chem Front* 2019;3:1317-22. DOI

17. Zhao Y, Wang F, Wang C, et al. Encapsulating highly crystallized mesoporous Fe_3O_4 in hollow N-doped carbon nanospheres for high-capacity long-life sodium-ion batteries. *Nano Energy* 2019;56:426-33. DOI
18. Wang C, Wang J, Hu W, Wang D. Controllable synthesis of hollow multishell structured Co_3O_4 with improved rate performance and cyclic stability for supercapacitors. *Chem Res Chin Univ* 2020;36:68-73. DOI
19. Yan Z, Jin H, Guo J. Low-temperature synthesis of graphitic carbon-coated silicon anode materials. *Carbon Energy* 2019;1:246-52. DOI
20. Zhang F, Cao H, Yue D, Zhang J, Qu M. Enhanced anode performances of polyaniline-TiO_2-reduced graphene oxide nanocomposites for lithium ion batteries. *Inorg Chem* 2012;51:9544-51. DOI PubMed
21. Chen Z, Chen J, Bu F, Agboola PO, Shakir I, Xu Y. Double-holey-heterostructure frameworks enable fast, stable, and simultaneous ultrahigh gravimetric, areal, and volumetric lithium storage. *ACS Nano* 2018;12:12879-87. DOI PubMed
22. Kim W, Hwa Y, Jeun J, Sohn H, Hong S. Synthesis of SnO_2 nano hollow spheres and their size effects in lithium ion battery anode application. *J Power Sources* 2013;225:108-12. DOI
23. Xie Q, Zhao Y, Guo H, et al. Facile preparation of well-dispersed CeO_2-ZnO composite hollow microspheres with enhanced catalytic activity for CO oxidation. *ACS Appl Mater Interfaces* 2014;6:421-8. DOI PubMed
24. Zhao H, Dong Y, Jiang P, Wang G, Zhang J. Highly dispersed CeO_2 on TiO_2 nanotube: a synergistic nanocomposite with superior peroxidase-like activity. *ACS Appl Mater Interfaces* 2015;7:6451-61. DOI PubMed
25. Zeng M, Li Y, Mao M, Bai J, Ren L, Zhao X. Synergetic effect between photocatalysis on TiO_2 and thermocatalysis on CeO_2 for gas-phase oxidation of benzene on TiO_2/CeO_2 nanocomposites. *ACS Catal* 2015;5:3278-86. DOI
26. Primo A, Marino T, Corma A, Molinari R, García H. Efficient visible-light photocatalytic water splitting by minute amounts of gold supported on nanoparticulate CeO2 obtained by a biopolymer templating method. *J Am Chem Soc* 2011;133:6930-3. DOI PubMed
27. Wu X, Niu H, Fu S, et al. Core-shell CeO_2@C nanospheres as enhanced anode materials for lithium ion batteries. *J Mater Chem A* 2014;2:6790. DOI
28. Wang X, Liu D, Song S, Zhang H. Pt@CeO_2 multicore@shell self-assembled nanospheres: clean synthesis, structure optimization, and catalytic applications. *J Am Chem Soc* 2013;135:15864-72. DOI PubMed
29. Hua C, Fang X, Yang Z, Gao Y, Wang Z, Chen L. Lithium storage mechanism and catalytic behavior of CeO_2. *Electrochem commun* 2012;25:66-9. DOI
30. Sasidharan M, Gunawardhana N, Yoshio M, Nakashima K. CeO_2 hollow nanospheres as anode material for lithium ion batteries. *Chem Lett* 2012;41:386-8. DOI
31. Wang G, Bai J, Wang Y, Ren Z, Bai J. Prepartion and electrochemical performance of a cerium oxide-graphene nanocomposite as the anode material of a lithium ion battery. *Scripta Materialia* 2011;65:339-42. DOI
32. Bai H, Liu Z, Sun DD. A lithium-ion anode with micro-scale mixed hierarchical carbon coated single crystal TiO_2 nanorod spheres and carbon spheres. *J Mater Chem* 2012;22:24552. DOI
33. Zhao B, Jiang S, Su C, et al. A 3D porous architecture composed of TiO_2 nanotubes connected with a carbon nanofiber matrix for fast energy storage. *J Mater Chem A* 2013;1:12310. DOI
34. Chen Y, Huang QZ, Wang J, Wang Q, Xue JM. Synthesis of monodispersed SnO_2@C composite hollow spheres for lithium ion battery anode applications. *J Mater Chem* 2011;21:17448. DOI
35. Han F, Li W, Li M, Lu A. Fabrication of superior-performance SnO_2@C composites for lithium-ion anodes using tubular mesoporous carbon with thin carbon walls and high pore volume. *J Mater Chem* 2012;22:9645. DOI
36. Liu B, Cao M, Zhao X, Tian Y, Hu C. Facile synthesis of ultrafine carbon-coated SnO_2 nanoparticles for high-performance reversible lithium storage. *J Power Sources* 2013;243:54-9. DOI
37. Zhu T, Chen JS, Lou XWD. Glucose-assisted one-pot synthesis of FeOOH nanorods and their transformation to Fe3O4@carbon nanorods for application in lithium ion batteries. *J Phys Chem C* 2011;115:9814-20. DOI
38. Ma Y, Zhang C, Ji G, Lee JY. Nitrogen-doped carbon-encapsulation of Fe_3O_4 for increased reversibility in Li^+ storage by the conversion reaction. *J Mater Chem* 2012;22:7845. DOI
39. Hui K, Fu J, Liu J, et al. Yolk-shell nanoarchitecture for stabilizing a Ce_2S_3 anode. *Carbon Energy* 2021. DOI
40. Massiot D, Fayon F, Capron M, et al. Modelling one- and two-dimensional solid-state NMR spectra: modelling 1D and 2D solid-state NMR spectra. *Magn Reson Chem* 2002;40:70-6. DOI
41. Oka R, Shobu Y, Aoyama F, Tsukimori T, Masui T. Synthesis and characterisation of $SrY_{2-x}Ce_xO_4$ as environmentally friendly reddish-brown pigments. *RSC Adv* 2017;7:55081-7. DOI
42. Pang H, Chen C. Facile synthesis of cerium oxide nanostructures for rechargeable lithium battery electrode materials. *RSC Adv* 2014;4:14872-8. DOI
43. Song Y, Chen Z, Li Y, et al. Pseudocapacitance-tuned high-rate and long-term cyclability of $NiCo_2S_4$ hexagonal nanosheets prepared by vapor transformation for lithium storage. *J Mater Chem A* 2017;5:9022-31. DOI
44. Song Y, Cao Y, Wang J, et al. Bottom-up approach design, band structure, and lithium storage properties of atomically thin γ-FeOOH nanosheets. *ACS Appl Mater Interfaces* 2016;8:21334-42. DOI PubMed
45. Shi Y, Tang M. NMR/EPR investigation of rechargeable batteries. *Acta Phys-Chim Sin* 2020;36:1905004. DOI
46. Tang M, Sarou-Kanian V, Melin P, et al. Following lithiation fronts in paramagnetic electrodes with in situ magnetic resonance spectroscopic imaging. *Nat Commun* 2016;7:13284. DOI PubMed PMC
47. Meyer BM, Leifer N, Sakamoto S, Greenbaum SG, Grey CP. High field multinuclear NMR investigation of the SEI layer in lithium rechargeable batteries. *Electrochem Solid-State Lett* 2005;8:A145. DOI